Structural and electronic properties of titanium dioxide

Keith M. Glassford and James R. Chelikowsky

Department of Chemical Engineering and Materials Science, Minnesota Supercomputer Institute,
University of Minnesota, Minneapolis, Minnesota 55455

Calculations have been performed using "soft-core" *ab initio* pseudopotentials constructed within the local-density approximation, and a plane-wave basis for the structural and electronic properties of titanium dioxide in the rutile structure. The ground-state structural and cohesive properties were obtained by self-consistently minimizing the total energy with respect to the structural parameters a, c, and u. Our calculated cohesive and structural properties at ambient pressure agree to within 5% and 1% of experimental values, respectively. The structural and elastic properties under pressure are also in good agreement with experiment. The interplay between ionic and covalent bonding between Ti and O is investigated through the valence-charge density and compared to experimental charge-deformation maps. The electronic band structure is found to be in good agreement with experimental results. We analyze the optical spectrum of rutile and obtain agreement with experiment away from the fundamental absorption edge. Our study suggests material properties for early-transition-metal oxides are well reproduced within the local-density approximation.

I. INTRODUCTION

Transition-metal oxides remain one of the most difficult classes of solids to perform material property predictions via "first-principles" or *ab initio* calculations. Oxides of interest often have complex structures containing many atoms per unit cell, as in the case of high-temperature superconductors such as $YBa_2Cu_3O_{7-x}$. Transition-metal oxides exhibit a wide range of behavior ranging from high-temperature superconductivity to insulators such as NiO, as well as wide- and narrow-band-gap semiconductors such as TiO_2 and Ti_2O_3. Experimentally, considerable work has been performed on transition-metal oxides. Reviews of the field include those by Gray,[1] Goodenough,[2] and Henrich.[3] However, little work has been performed theoretically owing to the intense computational requirements needed for self-consistent calculations for these complex materials. To perform realistic calculations, efficient computational schemes must be implemented to understand transition-metal oxides on a fundamental level.

Various approaches have been attempted for predicting the electronic and structural properties of condensed-matter systems from first principles. Most of these approaches use the local-density approximation (LDA) of Hohenberg, Kohn, and Sham[4] (HKS). This approach has experienced a considerable amount of success in predicting ground-state structural and cohesive properties of condensed-matter systems.[5-7] The LDA provides structural and elastic data in good agreement with experiment; lattice constants, bulk moduli, elastic constants, and phonon frequencies are usually predicted within 1–5% of experimental values.[8] For binding energies, the LDA consistently overestimates experimental values by approximately 15–20%. This discrepancy may be attributed to an incomplete cancellation of errors within the LDA.[5,9] In the case of optical properties, band gaps,

conductivities, and other properties involving excited states, the LDA is not expected to agree well with experiment as it is a ground-state formalism. Nonetheless, we find the LDA performs reasonably well in describing certain aspects of these excited-state properties for titania.

A simple approach in calculating the properties of crystalline materials is the incorporation of a plane-wave basis[10] to describe the electronic wave functions. This approach offers an attractive means for calculating the electronic and structural properties of solids,[10,11] quantum-mechanical forces and stresses,[8,10] *ab initio* molecular dynamics,[12] and quasiparticle excitations.[13] Another advantage in using a plane-wave basis is it forms a complete set. It is relatively simple to improve systematically the basis set by increasing the number of plane waves. Since plane waves form an orthogonal set, no explicit orthogonalization is required as in the case of a Gaussian or other localized basis set. Probably most important, plane waves are "shape preserving," i.e., all possible symmetries $s, p, d, f, \ldots$ are included in the basis set.

Until recently, it has been impractical to perform *ab initio* total-energy calculations for transition metals, or their oxides, using simple approaches such as combining a plane-wave basis and pseudopotentials. The strong localization of the valence d wave functions results in poor convergence when a modest number of plane waves is used in conjunction with traditional pseudopotential methods.[11] For transition-metal oxides, the calculations are also complicated by the fact that the O $2p$ valence wave function has no corresponding core states of the same angular momentum. Since the $2p$ state need not be orthogonal to the core, such states are localized in contrast to second-row elements such as sulfur. The recent development of methodologies for generating "soft" transferable pseudopotentials[14-16] as well as more efficient computational techniques[11,12,17] have resolved

STRUCTURAL AND ELECTRONIC PROPERTIES OF TITANIUM . . .

such issues and have made the plane-wave basis set an attractive means of solving the HKS equations.[4]

Our study of titania is motivated by a number of factors. The practical importance of titanium dioxide is illustrated by its use as a substrate in catalytic[18] and electrochemical processes,[19] and as a pigmentation for paints and polymers. The optical and electronic properties of TiO_2 have applications in gas-sensing devices, antireflection coatings for solar cells, a dielectric material for integrated electrons, as well as applications in photochemical energy-conversion processes.[20] Titanium dioxide has also attracted attention owing to its structural and chemical analogy with stishovite (SiO_2). As stishovite occurs in the rutile structure, it is believed that its high-pressure polymorphs, important for understanding the velocity of propagating waves through the earth's mantle, will have similar high-pressure polymorphs as TiO_2. Several issues[21,22] remain outstanding concerning the structure of the high-pressure phases of TiO_2. An understanding of the pressure-induced structural modifications prior to phase transition will provide information concerning the driving force behind these structural modifications.

Here, we present calculations performed for the structural, cohesive, electronic, and optical properties of TiO_2 in the rutile structure. These calculations were performed using *ab initio* pseudopotentials constructed within the LDA and a plane-wave basis in conjunction with newly developed diagonalization techniques.[11,17] These techniques make the plane-wave method an efficient alternative to current methods and are briefly reviewed in Sec. II. In Sec. III, we discuss the ground-state properties of the rutile structure as obtained by self-consistently minimizing the total energy with respect to the structural parameters a, c, and u. Variation of these parameters under pressure as well as the elastic properties are also discussed in this section. The electronic properties are discussed in Sec. IV. We examine the band structure, density of states, and valence-charge density, and compare our *ab initio* results to experiment. In Sec. V, we present calculations for the reflectivity and dielectric functions. We discuss in detail the structural features of the imaginary part of the dielectric function resulting from specific electronic excitations within the first Brillouin zone. Finally, the paper concludes with the key points being summarized in Sec. VI.

II. METHODS OF CALCULATION

The electronic and structural properties of TiO_2 were calculated within the framework of LDA for which the HKS equations are solved self-consistently. The exchange-correlation potential of Ceperley and Adler[23] as parametrized by Perdew and Zunger[24] has been used. Previous studies[11,25−29] have shown this methodology to yield accurate structural parameters, cohesive energies, bulk moduli, phase-transition pressures, and elastic constants for solid-state materials as well as for molecules and surfaces.[30]

The pseudopotentials used in our work were generated self-consistently by the method of Troullier and Martins[14]

and were transformed using the separation technique proposed by Kleinman and Bylander.[31] The above methodology produces "soft-core" pseudopotentials which greatly reduce the number of plane waves needed to achieve convergence in the calculated properties. The O pseudopotential, shown in Fig. 1(a), was generated from the atomic ground-state configuration $(2s^2 2p^4)$ with radial cutoffs of 1.45 a.u. for both s and p components. The O $2p$ potential was chosen as the local component of the pseudopotential, and the nonlocal d component was neglected owing to its high energy relative to the atomic $2s$ and $2p$ valence states. The Ti pseudopotential, shown in Fig. 1(b), was generated from the ground-state configuration $(4s^2 3d^2 4p^0)$ with radial cutoffs of 2.54, 2.96, and 2.25 a.u. for the s, p, and d components, respectively. The Ti $4s$ potential was chosen as the local component of the pseudopotential. Also, inherent in separating the pseudopotential via the Kleinman-Bylander transform is the possibility of generating "ghost" states.[32] We have verified that our choice of local components and core radii did not introduce any "ghost" states as well as providing good transferability over a wide energy range. The transferability of our pseudopotentials is illustrated in Fig. 2, where we show the corresponding logarithmic derivatives of the radial component of the wave function. As seen in this figure, we obtain good transferability over a wide energy range as well as an absence of any ghost states.

The HKS equations[4] were solved self-consistently using a fast iterative diagonalization technique.[11,17] One of the
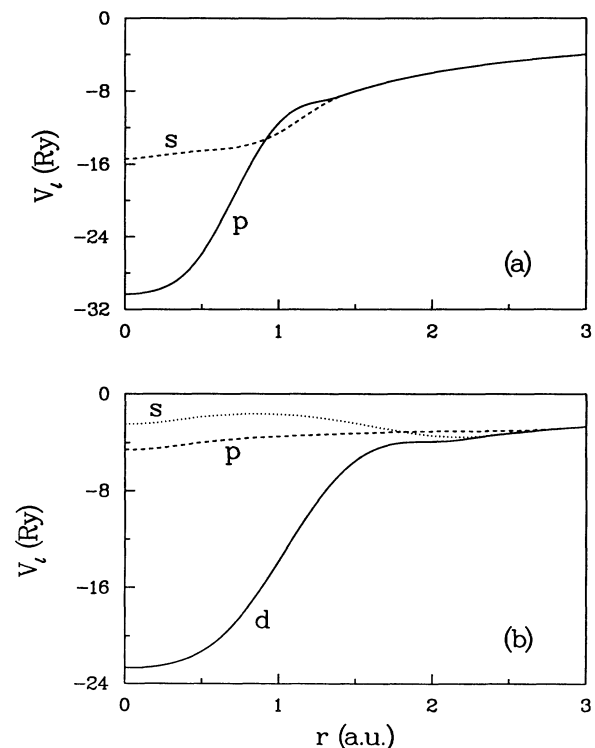

FIG. 1. Norm-conserving ionic pseudopotentials for (a) O $(2s^2 2p^4)$ and (b) Ti $(4s^2 3d^2 4p^0)$ generated using the recently developed method of Troullier and Martins (Ref. 14).
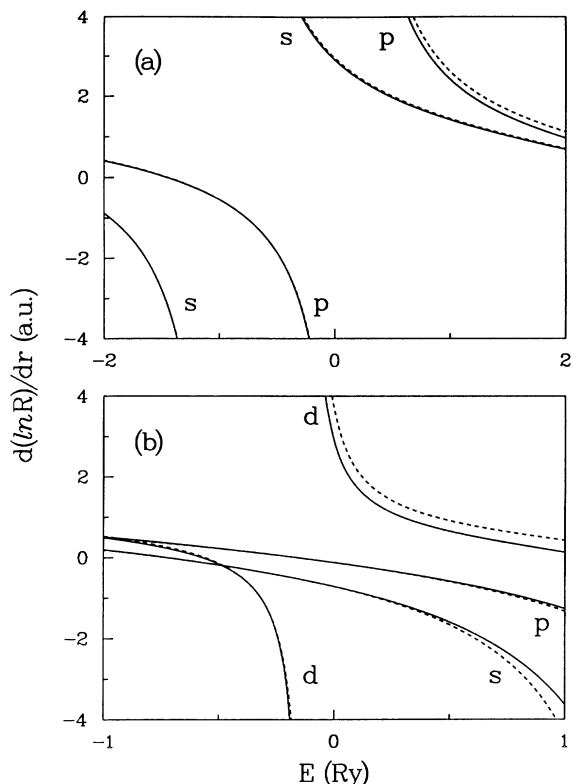
FIG. 2. Logarithmic derivatives of the radial wave functions $R(r)$ for the (a) O and (b) Ti wave functions for the all-electron (solid line) and pseudopotential results (dashed line) generated by the method of Troullier and Martins (Ref. 14) and a Kleinmann-Bylander (Ref. 31) transformation. The radial derivatives were generated at a radius of 1.8 a.u. for O and 2.81 a.u. for Ti.

major advantages of this method is that one does not need to calculate the full Hamiltonian matrix. Rather, only $H\psi$ needs to be calculated, leading to a drastic reduction in storage and increase in speed of computation. Plane waves up to an energy cutoff of $E_{cut} = 64$ Ry were included in the basis set, corresponding to ~ 3700 plane waves at the equilibrium geometry. Increasing this cutoff to $E_{cut} = 140$ Ry decreased the total energy per unit cell by only 20 mRy or 0.05 eV/atom. We have used one special k point in calculating the structural and electronic properties. To determine the sensitivity of the total energy on the k point sampling, we have increased the number of special k points to six, and find a total energy increase of only 0.05 eV/atom. Self-consistency was typically reached in nine iterations, where the Fourier components of the potential differed by less than 0.01 mRy from the previous iteration. At self-consistency, the total energy was stable to within 10^{-7} eV/atom or better between iteration cycles.

III. STRUCTURAL, COHESIVE, AND ELASTIC PROPERTIES

Titanium dioxide admits several polymorphic forms of which the rutile structure is the most common. Other naturally occurring polymorphs are the anatase, brookite,

ite, and the newly discovered $TiO_2(B)$ phase, which previously has only been synthesized using wet chemistry.[33] The tetragonal rutile structure belongs to the space group $P4_2/mnm$ (D_{4h}^{14}) and contains two TiO_2 molecules per primitive cell. The two Ti atoms are located at the Wycoff 2a sites: $(0,0,0;\frac{1}{2},\frac{1}{2},\frac{1}{2})$ with site symmetry D_{2h}, while the four O atoms are located at the 4f sites: $\pm(u,u,0;u+\frac{1}{2},\frac{1}{2}-u,\frac{1}{2})$ with site symmetry C_{2v}. The primitive unit cell is illustrated in Fig. 3(a), where the large and small spheres represent the O and Ti atoms, respectively. Each Ti atom is surrounded by a slightly distorted octahedron of O atoms, as shown by the dashed lines in the case of the central Ti atom. The octahedra centered at $(0,0,0)$ and $(\frac{1}{2},\frac{1}{2},\frac{1}{2})$ differ in orientation by a 90° rotation about the c axis with the oxygen atoms forming a hexagonal close-packed sublattice with half of the octahedral sites being filled by Ti atoms. For the various polymorphic forms of TiO_2, these TiO_6 octahedra form the basic structural unit. The major structural differences between TiO_2 polymorphs are the number of edge-shared octahedra, e.g., two in rutile, three in brookite, and four in anatase.[34] Consequently, in the case of rutile, one may visualize the structure as ribbons of these edge-shared octahedral aligned parallel to the principal axis, and joined at the corners by rotating each ribbon 90° about the c axis followed by a translation of $\pm\frac{1}{2}(a,a,c)$. This can be seen in Fig. 3(b), where we illustrate a projection of these ribbons onto the (110) plane, where the Ti

(a)
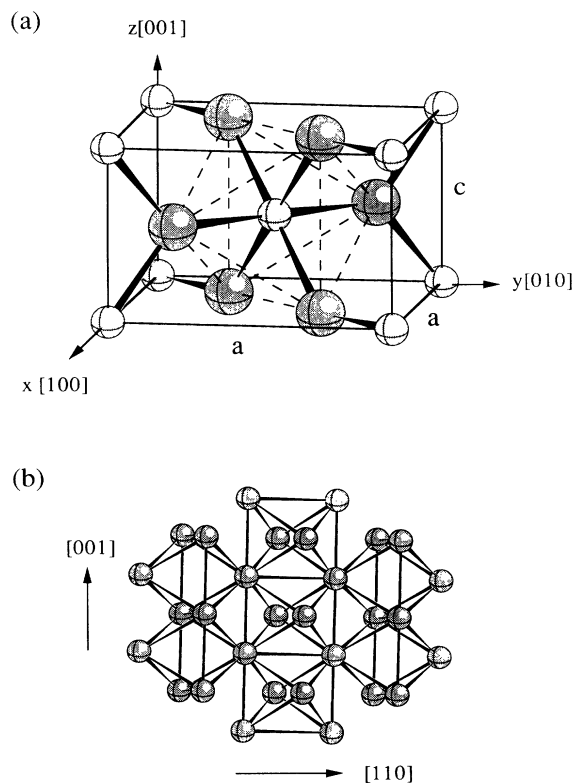

(b)

FIG. 3. Primitive unit cell for TiO_2 in the rutile structure (a); larger spheres represent the O atoms and the smaller Ti. In (b), we illustrate the connectivity of the oxygen octahedra projected onto the (110) plane; the Ti atoms have been omitted for clarity.

atoms have been removed for clarity.

The structural parameters for rutile have been determined to a high degree of accuracy from single-crystal x-ray-diffraction experiments performed by Abrahams and Bernstein.[35] Various other powder and single-crystal investigations have been performed using x-ray and neutron techniques to determine whether a shift in the oxygen positional parameter is present between these two techniques due to the polarizability of the oxygen atom.[36] Only a small difference in the oxygen positional parameter has been found between x-ray and neutron experiments.[36]

The distortion of the oxygen octahedra surrounding each Ti atom is governed by the internal parameter u, the axial ratio c/a, and a. Taking the principle axis of the octahedron, shown in Fig. 3(a), along the $[1\bar{1}0]$ direction, one may designate the two inequivalent Ti-O bonds, i.e., two apical bonds of length $au\sqrt{2}$, and four equatorial bonds of length $a[2(2u-1)^2+(c/a)^2]^{1/2}/2$. The apical and equitorial bonds are equal when u takes the special value of $u^*=\frac{1}{4}[1+\frac{1}{2}(c/a)^2]$. For $u>u^*$, the two apical bonds are larger than the corresponding equitorial bonds, and when $u<u^*$, the opposite is true. Perfect octahedral symmetry, however, would require lattice parameters of $(c/a)_{ideal}=2-\sqrt{2}\approx0.586$ and an internal parameter of $u_{ideal}=\frac{1}{2}(c/a)_{ideal}\approx0.293$, giving all twelve O-O bonds equal lengths. The experimental[35] values of u and c/a for TiO_2 indicate a slight elongation of the octahedra along its principle axis. This minimal distortion of the octahedra away from a regular structure results in the two apical bonds being slightly longer than the four equitorial bonds by $\sim2\%$. In fact, the values of u and c/a are very close to those which maximize the volume of the unit cell for equivalent Ti-O bonds where $c/a=\sqrt{2/5}\approx0.632$ and $u=\frac{3}{10}$ as determined by O'Keeffe.[37]

The ground state of the system is obtained by minimizing the total energy of the $P4_2/mnm$ structure with respect to the lattice parameters a, c, and u. We have performed this minimization by a two-step procedure. Specifying a unit cell volume, $V=ca^2$, we minimize the total energy with respect to c/a and u, using the calculated forces and stresses as a guide. This step is then repeated for other volumes near the proposed equilibrium structure. In Table I, we list the respective structural parameters and cohesive energies obtained in this fashion.
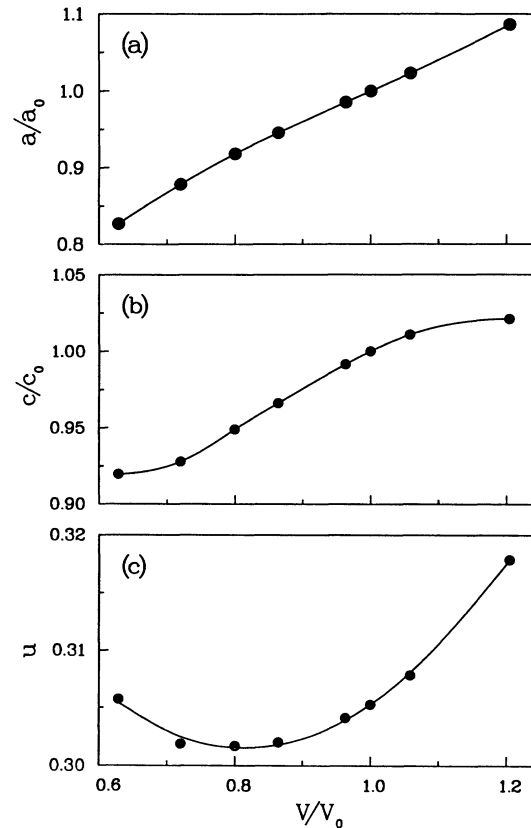

FIG. 4. Theoretical structural parameters (a), a, (b) c, and (c) u for the rutile structure based on ab $initio$ total-energy minimization for various reduced volumes. The values of a_0, c_0, and V_0 correspond to the minimum in the total energy, and are given in Table II. Closed circles refer to calculated values and the lines are a guide to the eye.

In Fig. 4, we illustrate the structural parameters as a function of the reduced volume V/V_0, where V_0 is the theoretical unit-cell volume at equilibrium. The corresponding energy-volume relationship is illustrated in Fig. 5, with the cohesive energy E_{coh} and the unit-cell volume given per TiO_2 molecule. The cohesive energy is defined as the difference between the total energy of the solid and the isolated pseudoatoms at zero temperature. The energies of the isolated pseudoatoms were found to be -429.59 and -89.88 eV for O and Ti, respectively.

TABLE I. Theoretical structural parameters and cohesive energy obtained by volume-constrained total-energy minimization. Volumes and cohesive energies are per TiO_2 molecular unit.

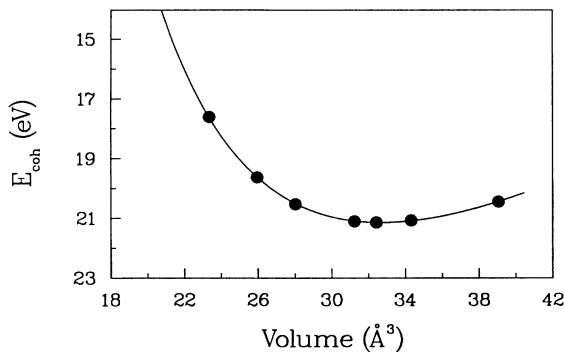| V (Å^3)	c (Å)	a (Å)	u	c/a	E_{coh} (eV)
20.375	2.733	3.862	0.305 73	0.7076	13.326
23.206	2.757	4.103	0.301 87	0.6701	17.611
25.932	2.820	4.289	0.301 68	0.6575	19.637
28.007	2.871	4.417	0.302 00	0.6500	20.533
31.225	2.946	4.604	0.304 12	0.6400	21.107
32.417	2.971	4.671	0.305 27	0.6362	21.143
34.305	3.004	4.779	0.307 83	0.6285	21.076
39.046	3.034	5.073	0.317 85	0.5980	20.453

FIG. 5. Theoretical equation of state for the TiO_2 rutile structure based on a Vinet et al. (Ref. 41) fit (solid line) and the corresponding theoretically calculated values (closed circles). Cohesive energies and volume are per TiO_2 molecular unit.

These values include a spin-polarization correction[38] of 1.41 and 0.68 eV for O and Ti using the corresponding spin-polarized exchange-correlation potentials.[23,24] The ground-state structure is obtained by minimizing the total energy of the system with respect to volume. Commonly, this is performed by fitting the theoretical values of energy and volume to an integrated equation of state (EOS), the most common being the Murnaghan[39] and the Birch-Murhaghan[40] forms, which are based on the elastic properties of the solid. Recently, another form has been proposed by Vinet et al.[41] which is based upon the cohesive properties of the solid.

In Table II, we compare the calculated structural, elastic, and cohesive properties as obtained by the Vinet et al.[41] EOS to the experimental values. The structural properties are in good agreement, being within 1% of the room-temperature experimental results of Abrahams and Bernstein.[35] This is expected, as structural properties are typically insensitive to errors within the LDA: the cancellation of errors between solid phases is usually quite good. However, for cohesive energies which do not involve differences between solid phases, incomplete cancellations associated with the LDA become more important:

TABLE II. Comparison of the experimentally determined structural (Ref. 35), cohesive (Ref. 42), and elastic parameters (Ref. 45) for TiO_2 in the rutile structure with the present theory. See text for definition of symbols.

Property	This work	Experiment
E_{coh} (eV/TiO_2)	21.1	19.9
V_0 (Å^3/TiO_2)	32.42	31.217
a (Å)	4.653	4.5936
c (Å)	2.965	2.9587
c/a	0.637	0.6441
u	0.305	0.3048
B_0 (GPa)	240	216
B_0'	4.63	6.76
$\beta_\perp$ (10^{-3} GPa^{-1})	1.918	1.936
$\beta_\parallel$ (10^{-3} GPa^{-1})	0.903	0.870
μ	0.281	0.278

cohesive energies are frequently $\sim 15\%$ larger than experiment.[9] In the present calculations, we find a cohesive energy which is approximately 5% larger than the experimental value. The experimental cohesive energy reported in Table II was calculated using the heat of formation for TiO_2 of -228.4 kcal/mole, a cohesive energy for Ti of 111.8 kcal/mole, and a dissociation energy for O_2 of 119.1 kcal/mole.[42,43] We have not considered thermal or vibrational contributions, e.g., zero-point motion, to the structural and cohesive properties, since these are expected to be much less than the inherent errors from the LDA. Further, experimental results[44] have shown the structural properties to be relatively insensitive to temperature. We note that the structural and cohesive properties obtained by the Murnaghan[39] and Birch-Murhaghan[40] EOS's are virtually identical to those obtained from the Vinet et al.[41] EOS reported in Table II.

In addition to the ground-state volume and cohesive energy, one may obtain elastic properties from the integrated EOS; specifically, the zero-pressure isothermal bulk modulus B_0 and its pressure derivative B_0'. We find an isothermal bulk modulus of 240 GPa, which, as in the case of the structural properties, is nearly independent of the chosen EOS. This value may be compared to single-crystal ultrasonic experiments[45] which find a value of 216 GPa at ambient conditions. To estimate the effects of temperature on B_0, we have taken the low-temperature elastic constant measurements[46] from 80 to 180 K and quadratically extrapolated B_0, i.e., $B_0 = \frac{1}{9}[c_{33} + 4c_{13} + 2(c_{11} + c_{12})]$ for D_{4h} symmetry, to absolute zero. The extrapolated value of 239 GPa is in excellent agreement with our ground-state calculations of 240 GPa, which are subsequently valid only at 0 K. While all three mentioned EOS's yield virtually the same bulk modulus, cohesive energy, and structural properties, we find differences between the calculated values of B_0'. For the Murnaghan,[39] Birch-Murnaghan,[40] and Vinet et al.[41] EOS's, we find B_0' values of 3.82, 4.32, and 4.63, respectively. Compared to the experimental value of 6.84, obtained by single-crystal ultrasonic experiments,[45] our EOS fits yield values of B_0' which are too small. The disparity between the pressure derivatives is not unexpected, owing to the experimental difficulty in obtaining accurate values, as well as differences in the fitting procedure used.

The experimental[47−49] P-V results are shown in Fig. 6, and are compared to our theoretical EOS. We note that shock-wave experiments[50,51] find a strong variation in the transition pressure with the direction of the propagating shock wave; we only show experimental values prior to the transition pressure of ~ 30 GPa for the [001] direction.[47,50,51] As shown in Fig. 6, the theoretical EOS generally predicts larger unit-cell volumes than those found experimentally. However, if one takes the experimental data[47−49] shown in Fig. 6, and fits the P-V data to the Vinet et al.[41] EOS, one finds values of B_0 and B_0' corresponding to 212 GPa and 4.34, respectively. In Fig. 6 we show the corresponding EOS by the dashed line. While this bulk modulus is in good agreement with the experimental results given in Table II, the resulting value of B_0' is in disagreement with the experimental results.[45] The
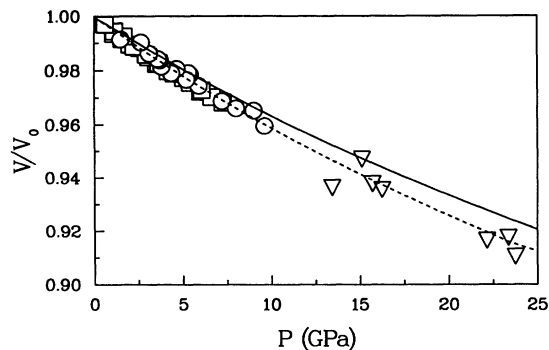
FIG. 6. Comparison between the theoretical P-V relationship and experiment: open circles (Ref. 48), squares (Ref. 49), and triangles (Ref. 47). The solid line corresponds to the Vinet et al. (Ref. 41) EOS fit to the present results, and the dotted line is the best fit to the combined experimental (Refs. 47–49) results.

discrepancy between experiment and theory may thus be due to the low pressures used in previous experiments, as the combined low- and high-pressure experiments yield a value of B_0' in good agreement with the present results.

Another important elastic property, along with B_0 and B_0', is the Poisson ratio for uniaxial stress applied along
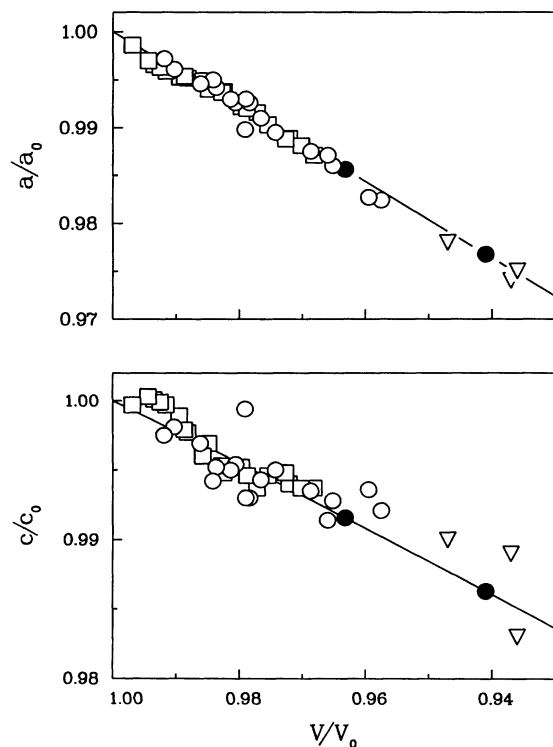

FIG. 7. Comparison of pressure-induced variations in the structural parameters a and c compared to experimental results. Closed circles represent our present results, while the open circles (Ref. 48), squares (Ref. 49), and triangles (Ref. 47) pertain to experimental values. The solid line is included as a guide to the eye and corresponds to that illustrated in Fig. 4.

the c axis, μ, and is given by $\mu = -d \ln a / d \ln c$. Near the equilibrium structure, we have calculated the value of a and u as a function of c by minimizing the total energy. Our theoretical value of the Poisson ratio is $\sim 1\%$ larger than the experimental value given in Table II.

In Fig. 7, we compare our theoretical lattice parameters a and c as given in Table I to the experimental results of TiO_2 under pressure.[47–49] As seen from this figure, our results are in good agreement with the experimental values for a. In the case of c, however, a significant degree of uncertainty exists in the experimental results. Nonetheless, our theoretical predictions are within the experimental scatter. From the volume derivatives of a and c from Fig. 7, and our theoretical EOS, we have determined the zero-temperature bulk linear compressibilities perpendicular, $\beta_\perp = -d \ln a / dP$, and parallel, $\beta_\parallel = -d \ln c / dP$, to the c axis. The resulting linear compressibilities are given in Table II and are in good agreement with the room-temperature single-crystal ultrasonic experiments.[45] We attribute the small discrepancy of our calculated $\beta_\parallel$ to experimental difficulties in the x-ray experiments, evident in Fig. 7, as well as temperature effects. From these values a large anisotropy is observed, with $\beta_\perp / \beta_\parallel \gtrsim 2$. The anisotropy has been attributed to the cation-cation repulsion along the ribbons parallel to the c axis.[52,53] For the oxygen positional parameter we are aware of only one experimental study in which the oxygen positional parameter u has been determined under pressure.[52] However, as in the case of c, a significant amount of scatter in the experiment is present.

IV. ELECTRONIC STRUCTURE

The electronic structure of titania has been experimentally probed by x-ray photoemission spectroscopy[54–56] (XPS), x-ray-induced Auger-electron spectroscopy,[54] Auger-electron spectroscopy,[57] x-ray emission[58,59] (XES) and absorption spectroscopy[60–62] (XAS), electron-energy-loss spectroscopy[54,63–65] (EELS), ultraviolet photoelectron spectroscopy[66,67] (UPS), and resonant photoelectron spectroscopy[68] (RUPS). Accurate, self-consistent ab initio electronic structure calculations for TiO_2 have only recently become available. Self-consistent total-energy calculations have been performed within the LDA using a pseudopotential plane-wave formalism[69,70] as well as the more recent Hartree-Fock pseudopotential calculation.[71] Self-consistent calculations using the linear muffin-tin orbital (LMTO) method[72–74] have also recently been performed in an attempt to understand the near-edge structure in core-level spectroscopies. Prior to these studies, theoretical calculations have largely centered around more empirical methods, e.g., $X\alpha$ cluster calculations,[75] tight-binding[76–79] (TB) calculations, and the extended Hückel molecular-orbital method.[65]

A. Band structure

Using the theoretical lattice parameters given in Table II, we have calculated the self-consistent band structure, shown in Fig. 8, along the high-symmetry directions of the irreducible Brillouin zone (BZ) (see Fig. 9). The ener-
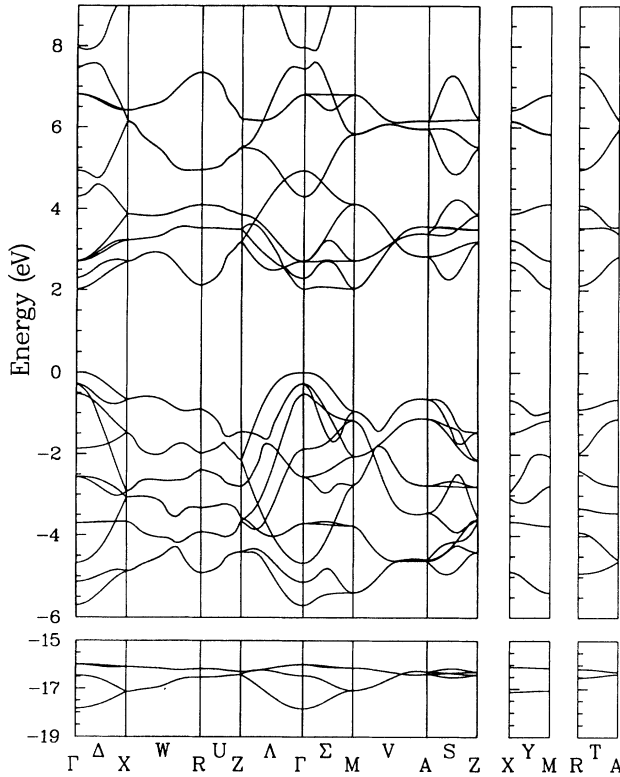
FIG. 8. Band structure for TiO_2 along high-symmetry directions of the irreducible Brillouin zone. The valence-band maximum is taken as the energy zero.

gy zero has been taken as the valence-band maximum. The bands shown in the lower panel results from predominantly O $2s$ character with a width of ~ 1.8 eV. The upper valence bands are composed mainly of O $2p$ states hybridized with Ti $3d$ character. The resulting bandwidth of 5.7 eV is in good agreement with experimental XPS,[54–56] UPS,[66–68] and XES (Ref. 58) measurements, which are in the range of 5–6 eV. The separation between the O $2s$ valence states and the minimum of the conduction band occurring at Γ was found to be approxi-
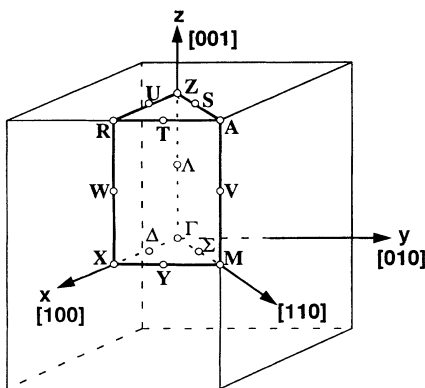

FIG. 9. Symmetry labels for the irreducible Brillouin zone of the tetragonal Bravais lattice.

mately 17 eV and is consistent with Auger[57] and x-ray-photoemission[58,55] spectroscopies, which place the separation at about 16–18 eV. The present calculations predict a *direct-forbidden* gap at Γ of 2.0 eV, i.e., the direct gap at Γ is dipole forbidden. As expected, the LDA gap is $\sim 33\%$ lower than the experimental value[80,81] of 3.0 eV.

A considerable discrepancy exists both theoretically and experimentally concerning the conduction-band minimum. Early experimental investigations were based upon transport properties, which, owing to the low-carrier mobilities, were usually performed with reduced or doped samples. Becker and Hosler[82] proposed a multivalley conduction-band minimum based upon Hall-effect measurements. In their model, the lowest conduction band occurs at Γ, and the second band, located away from the zone center, occurs ~ 50 meV higher in energy. Acket and Volger,[83] on the other hand, have proposed a one-band multivalley conduction-band minimum to explain the anisotropy of the Hall and Seeback coefficients, initially assigning the minimum along the Δ direction. Piezoresistivity measurements by Bir *et al.*[84] have inferred a nondegenerate conduction-band minima located along Λ in support of the single-band multivalley interpretation of Ackert and Volger.[83] These experiments, however, are strongly dependent upon sample preparation, temperature, and defect concentration. Perhaps the most direct way to determine the lowest conduction-band minimum is via optical experiments which measure the excitations across the optical gap. Accurate absorption[80,85] and wavelength-modulated transmission[86] spectroscopic studies have determined that TiO_2 is a direct-forbidden-gap semiconductor, i.e., the direct transition is dipole forbidden, in agreement with our calculations. The indirect-allowed transition which is dipole allowed was found to be nearly degenerate with the direct-forbidden transition with a corresponding separation of ~ 15 meV (Refs. 80 and 86), and is in agreement with the original interpretation proposed by Becker and Hosler.[82]

Early theoretical work based on TB (Ref. 77) and LMTO (Ref. 87) calculations has predicted an indirect gap from $\Gamma \rightarrow M$. Likewise, recent Hartree-Fock calculations[71] also predict an indirect transition from $\Gamma \rightarrow M$, with an almost-degenerate conduction-band minimum occurring at Γ; however, the resulting band gap of ~ 10 eV is larger than experiment by a factor of 3. Recent LMTO calculations[73,74] yield conflicting results. The calculations performed by Khan, Kotani, and Parlebas[73] find an indirect transition from Γ to a point near R, while those of Poumellec, Durham, and Guo[74] find results which are in good agreement with our present calculations, the major difference being the ordering of the upper valence bands at Γ resulting in a doubly degenerate valence-band maximum. We also find a conduction-band state located at M which is approximately 10 meV above the conduction-band minimum at Γ. This difference is in good agreement with the experimentally[80,86] observed separation of 15 meV between the direct and indirect gaps, although such a small energy difference is probably beyond the accuracy of the present calculations. The LMTO calculations by Poumellec, Durham, and Guo[74]

STRUCTURAL AND ELECTRONIC PROPERTIES OF TITANIUM . . .

find a similar separation of ~30 meV. Hartree-Fock calculations[71] also find a small energy difference between the conduction-band minima at Γ and M, the minima being reversed from the LDA calculations.

The lower conduction bands, composed primarily of unoccupied Ti $3d$ states, have a full width of 5.6 eV and may be divided into two distinct groups. These two groups are reminiscent of the crystal-field splitting of the Ti $3d$ states of the TiO_6^{8-} ion into the triply degenerate t_{2g} and doubly degenerate e_g states. In the case of TiO_2, the perfect O_h symmetry of the Ti site is lowered to D_{2h}, which further splits these states into the singly degenerate $\{b_{3g}, a_g, b_{2g}\}$ and $\{b_{1g}, a_g\}$ states, respectively.[88] The lower group of states has a bandwidth of 2.9 eV with an average energy of 3.5 eV and may be associated with states of t_{2g} symmetry. The upper conduction bands associated with states of e_g symmetry have a width of 3.3 eV with an average energy of 6.0 eV. Other than a small overlap between these two groups at ~4.6 eV, the t_{2g} and e_g bands remain reasonably well separated over the entire BZ. The separation between the centers of these two groups was found to be 2.5 eV. This separation is only a rough estimate, as further splitting is observed due to the distortion of the O_h crystal field to D_{2h} as previously mentioned. Nonetheless, the splitting is comparable to experimental XAS (Refs. 58, 60, 62, 63, and 59) and EELS (Refs. 63 and 65) measurements which place the separation between 2.1 and 3.0 eV. Similar features between these two complexes have also been observed in the LMTO calculations of Poumellec, Durham, and Guo[74] and by Medvedeva et al.[72] However, the calculations of Khan, Kotani, and Parlebas[73] find a forbidden t_{2g}-e_g gap of ~3 eV, which is inconsistent with the above calculations as well as with experiment. We note that the results obtained in the present study are consistent with both experimental XAS results[60] and self-consistent LMTO calculations of other transition-metal oxides crystallizing in the rutile structure.[89]

B. Density of states

In Fig. 10, we show the density of states (DOS) for TiO_2 in the rutile structure. The DOS was calculated using the linear analytic tetrahedron method[90] to evaluate the integrals over the constant-energy surfaces. We have performed self-consistent calculations at 126 k points in the irreducible BZ and have taken the valence-band maximum as the energy zero. The theoretical DOS has been convoluted with a Gaussian with a half-width at half maximum of 0.15 eV to account for the finite sampling grid and experimental resolution.

Valence-band spectra have been experimentally determined using XPS,[54–56] XES,[58,59] and UPS (Refs. 66–68) measurements. In Fig. 10, we show the valence-band density of states obtained from RUPS (Ref. 68) on the $TiO_2(110)$ surface at a photon energy of 46 eV. Similar features have been previously obtained by XPS (Ref. 56) and UPS (Ref. 66) with splittings between the two major peaks ranging from 1.7 to 2.0 eV. The center-to-center separation of our theoretical peaks of 2.4 eV is in good agreement with the experimental[68] results. We note that
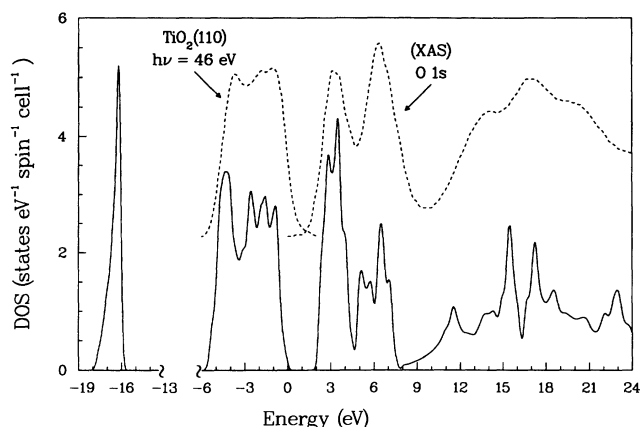

FIG. 10. Density of states for TiO_2 given in states per eV, per spin, and per unit cell (solid line) compared to experimental UPS (Ref. 68) for the TiO_2 (110) surface at a photon energy of 46 eV and the TiO_2 XAS (Ref. 61) spectra of the O $1s$ edge. The valence-band maximum has been taken as the energy zero for the theoretical results, which have been convoluted with a Gaussian of half-width at half maximum of 0.15 eV to account for finite sampling grid and experimental resolution.

the major features of the valence band have been found to be relatively insensitive to surface effects.[3] This has been theoretically shown in the tight-binding calculations[76] in which differences between the bulk and surface DOS's were found to be negligible.

Recent experimental investigations probing the unoccupied conduction-band states in transition-metal oxides have centered around XAS (Refs. 60–62) and EELS (Refs. 54 and 63–65) measurements. At low momentum transfer, the resulting spectra may be approximated as images of the local conduction-band character based on selection rules between initial and final states, e.g., $\Delta l = \pm 1$. The O $1s$ XAS spectra may be approximated as the oxygen p-projected density of states of the conduction band. In Fig. 10, we compare our theoretical DOS to the O $1s$ XAS results of van der Laan[61] (dashed line). While the intensities of various structural details may change due to matrix element effects, our theoretical results are in good agreement with experiment. The first two peaks are a result of the crystal-field splitting of the Ti $3d$ wave functions into states with t_{2g} and e_g symmetries. These states represent, respectively, the π and σ Ti d orbitals hybridized with O $2p$ states, the σ-e_g orbitals being higher in energy. The DOS between 9 and 24 eV is primarily of Ti $4sp$ character[60,61] and is well reproduced by the present calculations. Owing to our smaller band gap from the LDA, we have aligned the experimental and theoretical curves with the center of the first major peak at ~3.2 eV. Similar features have also been observed in the Ti $L_{2,3}$ edge from EELS (Ref. 63) and XAS (Ref. 61) experiments which represent the conduction-band Ti $3d$ character.

C. Electron density

Simple oxides, such as MgO, are predominantly ionic insulators with spherically symmetric charge densities

about each ion. The participation of d orbitals in the electronic properties of transition-metal oxides results in a significant degree of covalent character and a distortion of the atomiclike charge density surrounding the transition-metal ion. In order to characterize the degree of covalent bonding in TiO_2, we have calculated the deformation electron density based on the *independent-atom* model. In this model, one defines $\Delta\rho(r)$ as the difference between the total valence electron density and linear superposition of radially symmetric atomic charge densities. In regions of positive deformation, charge buildup occurs and corresponds to "bonding" electrons, while regions of negative deformation corresponds to "antibonding" states. The relative displacement of the maximum in $\Delta\rho$ towards the more electronegative atom indicates the degree of ionic bonding, or, more loosely, the charge transfer from the cation to the anion. Pauling[34] has proposed that edge-shared polyhedra decrease the stability of an ionic crystal. One therefore expects a significant degree of covalent character between the Ti-O bonds in order to compensate for a reduced stability accompanying the shared edges of the oxygen octahedra.[1] This would result in regions of positive charge deformation along and perpendicular to the Ti-O bonds.

In Figs. 11(a) and 11(b), we show contour plots of the valence, or "pseudo-charge," deformation maps for the (110) and ($\bar{1}$10) planes of the tetragonal unit cell. Positive and negative deformation densities are indicated by the solid and dashed contours, respectively. The (110) plane contains the two apical bonds, while the ($\bar{1}$10) plane contains the four equitorial bonds. Spherical pseudoatomic
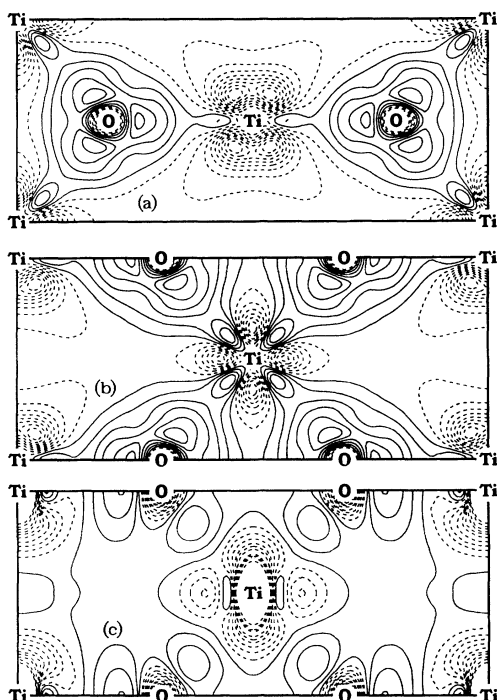

FIG. 11. Pseudoatom valence density difference maps for the (a) (110) and (b) ($\bar{1}$10) lattice planes. Contours of constant charge density are separated by $3e/V_0$. In (c) we show the experimental (Ref. 92) electron density map in the ($\bar{1}$10) plane.

charge densities, taken from atomic calculations using the same ion core *ab initio* pseudopotentials as for the solid state, were used in constructing $\Delta\rho$. For the ($\bar{1}$10) plane, one can identify threefold-coordinated oxygen atoms with site symmetry C_{2v}, while the D_{2h} site symmetry of the Ti atom is evident from the distortion of the lobes of negative deformation along the [001] direction. The most prominent feature of these figures is the considerable degree of covalent character present in the Ti-O bonds. For the ionic model, one usually characterizes the Ti ions as $3d^0$ with complete charge transfer to the O atoms. The failure of the ionic model to predict adequately the structural properties of TiO_2 indicates that covalent bonding must be taken into account.[79] We can approximate the degree of covalent character of the Ti-O bond using Pauling's[91] ionicity scale. Based on the electronegativity difference between Ti and O, one estimates $\sim 40\%$ covalent character in the Ti-O bond. This covalency is reflected in the charge-deformation maps and results from hybridization between the O $2p$ and Ti $3d$ wave functions. The participation of Ti $3d$ character in the bonding is also present in the band picture where a significant amount of Ti $3d$ character is contained in the O $2p$ valence band. Experimental evidence for this interpretation occurs in resonant photoemission studies where the photon energy is swept through the Ti $3p \rightarrow 3d$ optical transition energy.[68]

In Fig. 11(c), we show the experimental electron-deformation maps[92] for the ($\bar{1}$10) plane. Although variations in experimental deformation maps occur depending on the refinement model used, the major features include a significant degree of covalent character along the Ti-O bonds and regions of charge depletion around the Ti sites, elongating along the [001] direction towards nearest-neighbor Ti atoms.[92] We note that our pseudopotential calculations include only *valence* electrons, while the experimental charge-density difference maps are based on subtracting a superposition of theoretical atomic charge densities from the measured total charge density. Thus, the "experimental" difference map contains *total* charge densities, i.e., valence plus core charge densities. The pseudopotential difference maps contain the valence charge only. This is not a serious difficulty, as we are interested in the valence charge away from the core where the pseudopotential approach is known to provide good agreement with experiment.[93] Also, we do not expect significant changes within the core. Taking into account the variation between refinement models for the experimental results,[92] qualitative agreement is obtained between theory and experiment [Figs. 11(b) and 11(c), respectively].

In Figs. 12 and 13, we illustrate contour plots of the pseudo-charge density in the (110) plane and ($\bar{1}$10) planes, respectively. In (a) and (b) we show the e_g and t_{2g} conduction-band complexes, while (c) illustrates the charge density resulting from the upper-valence-band states of predominantly O $2p$ character. A prominent feature of these figures is the significant amount of charge residing on the O atoms in the conduction-band states as well as the Ti charge in the valence band. The higher-energy antibonding e_g-derived bands which are Ti-O σ
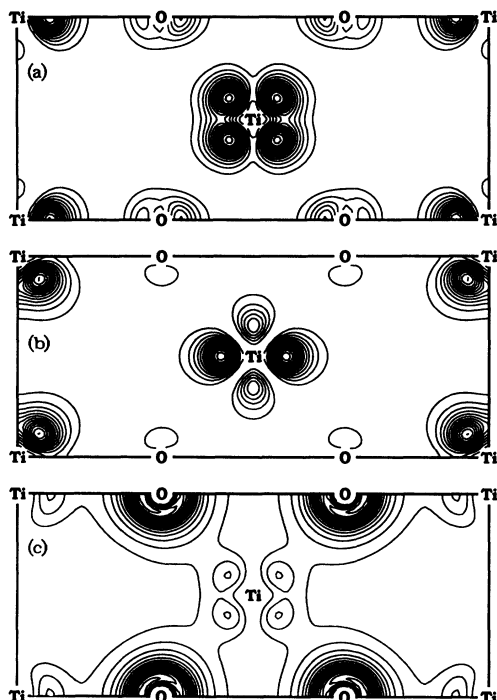
FIG. 12. Pseudo-charge-density contour plot of the (a) e_g, (b) t_{2g}, and (c) upper O $2p$ valence bands in the (110) lattice plane. Contours of constant charge density are separated by $10e/V_0$.
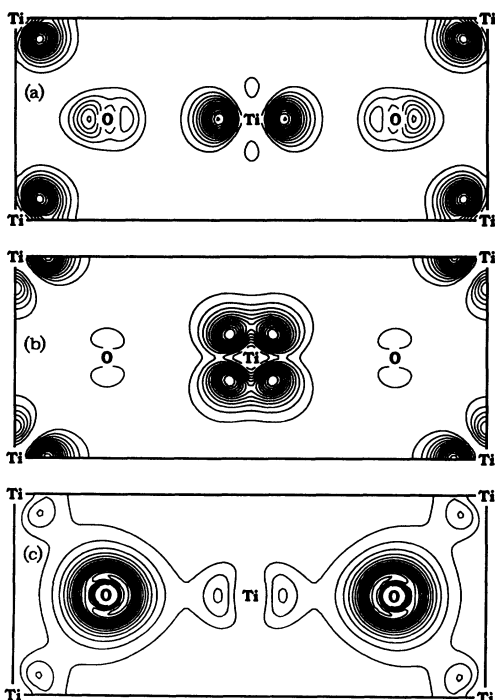

FIG. 13. Pseudo-charge-density contour plot of the (a) e_g, (b) t_{2g}, and (c) upper O $2p$ valence bands in the ($\bar{1}$10) lattice plane. Contours of constant charge density are separated by $10e/V_0$.

bonding, and the lower-energy t_{2g}-derived antibonding π-like bands are clearly discernible in these figures.

V. OPTICAL PROPERTIES

The optical properties of TiO_2 have been measured using reflectance,[94] electroreflectance,[95,96] absorption,[80,85] electroabsorption,[81] and wavelength-modulated transmission[86] spectroscopies. A considerable amount of fine structure has been observed in these experiments. The interpretation and assignment of experimentally observed spectral features to specific electronic excitations within the BZ depends upon accurate electronic structure calculations.

Excited-state properties, such as the dielectric function, become questionable within the HKS formalism as it is strictly a ground-state theory. However, the resulting HKS eigenvalues and eigenvectors are often associated with single-particle excitation energies and wave functions. For semiconductors and insulators, this association leads to band gaps which are often 30–50 % lower than experiment[13] and may be attributed to the ground-state formalism of the HKS approach.[97] To go beyond this single-particle description, one must incorporate the many-body nature of the electron-electron interactions, and correct for the incomplete cancellation of terms, which causes the electron to interact unphysically with itself. Formalism which account for these many-body effects, such as the quasiparticle[13] and self-interaction-correction approaches,[98,99] have met with reasonable success, i.e., within ∼0.1 eV, in describing excited-state properties for simple semiconductors and insulators. For simple insulators and semiconductors, these calculations result in wave functions which are virtually identical to those obtained with the LDA.[13] Here, we find the LDA can give good results for the optical properties of early-transition-metal oxides. Transition-metal oxides are known to be very difficult to model using the LDA, as exemplified by NiO, which the LDA predicts to be a metal rather than an insulator.[98] Until calculations such as these, it was problematic whether reasonable results could be obtained for the optical properties of any transition-metal oxide.

The standard theoretical approach in analyzing the influence of an external field on the electronic properties of a solid is through a response function. The response function for the optical properties of a solid, describing the absorption or emission of electrons or photons, is the dielectric function. One may calculate the dielectric function from accurate band-structure calculations, thereby allowing one to assign the spectral features to specific excitations within the BZ, as well as obtaining interband topologies. A successful application of this approach to the optical properties of diamond- and zinc-blende-structure semiconductors is the empirical pseudopotential method.[93] While this method has helped form much of our understanding of the optical properties of diamond- and zinc-blende-structure semiconductors, this method becomes increasingly difficult to implement for

insulators and materials with complex structures, and pseudopotentials, as is typical of many transition-metal oxides. An alternative method is to proceed with an *ab initio* method based on the LDA with the hope that the conduction bands will be at least qualitatively reproduced. For many tetrahedrally coordinated semiconductor systems, this is the case.[13,93]

The frequency-dependent dielectric function $\epsilon(\omega) = \epsilon_1(\omega) + i\epsilon_2(\omega)$ is evaluated using the formalism of Ehrenreich and Cohen.[100] In this procedure, the imaginary part of the dielectric function is given as

$$\epsilon_2(\omega) = \frac{4\pi^2 e^2 \hbar}{m^2 \omega^2} \sum_{v,c} \frac{2}{(2\pi)^3} \int_{BZ} \delta(\omega_{cv}(\mathbf{k}) - \omega)$$
$$\times |M_{cv}(\mathbf{k})|^2 d^3k \, , \quad (1)$$

where the integral is over the first Brillouin zone, $M_{cv}(\mathbf{k}) = \langle u_{c\mathbf{k}}|\hat{e}\cdot\nabla|u_{v\mathbf{k}}\rangle$ are the dipole matrix elements for the direct transitions between valence- and conduction-band states, $\hbar\omega_{cv}(\mathbf{k}) = E_{c\mathbf{k}} - E_{v\mathbf{k}}$ is the excitation energy $\hat{e}$ is the polarization vector of the electric field, and $u_{c\mathbf{k}}(\mathbf{r})$ is the periodic part of the Bloch wave function for a conduction-band state with wave vector $\mathbf{k}$. The physical significance of Eq. (1) may be realized by noting that the δ function accounts for energy conservation, while the matrix elements determine the allowed transitions through dipole selection rules. We have self-consistently determined the eigenvalues and wave functions at 126 $\mathbf{k}$ points within the irreducible part of the BZ (or $\frac{1}{16}$ of the full BZ). Matrix elements were calculated from the self-consistent wave functions and appropriately symmetrized over the BZ. Excitation energies between the valence- and conduction-band states up to approximately 25 eV from the valence-band edge were considered. Brillouin-zone integrations have been performed within the linear analytic tetrahedron scheme[90] by including the $\mathbf{k}$ dependence of the matrix elements up to first order.[101] The energy spacing was taken as 0.05 eV.

Owing to the large anisotropic nature of tetragonal cell of rutile, the optical properties are strongly dependent on the direction of the incoming polarized light. When the polarization direction is perpendicular ($\mathbf{E}_\perp$) or parallel ($\mathbf{E}_\parallel$) to the c axis, a high degree of fine structure exists in the optical properties.[94] Relating these structural features to critical points and interband topology within the BZ via Eq. (1) depends upon accurate band-structure calculations.

The imaginary part of the dielectric function for both $\mathbf{E}_\perp$ and $\mathbf{E}_\parallel$ polarizations is shown in Figs. 14(a) and 14(b), respectively. To account for finite sampling errors, the theoretical curves have been convoluted with a Gaussian with a half-width at half maximum of 0.15 eV. The experimental values of ϵ_2 for both $\mathbf{E}_\perp$ and $\mathbf{E}_\parallel$ have been determined by Cardona and Harbeke[94] from reflectance measurements and by Vos and Krusemeyer[96] using electroreflectance spectroscopy. While both experiments yield peak positions in reasonable agreement, their amplitudes are at variance. We have chosen to compare our theoretical result to the experimental work of Cardona and Harbeke,[94] which are in better agreement with other experimental observations.[102] In Figs. 14(a) and 14(b), we
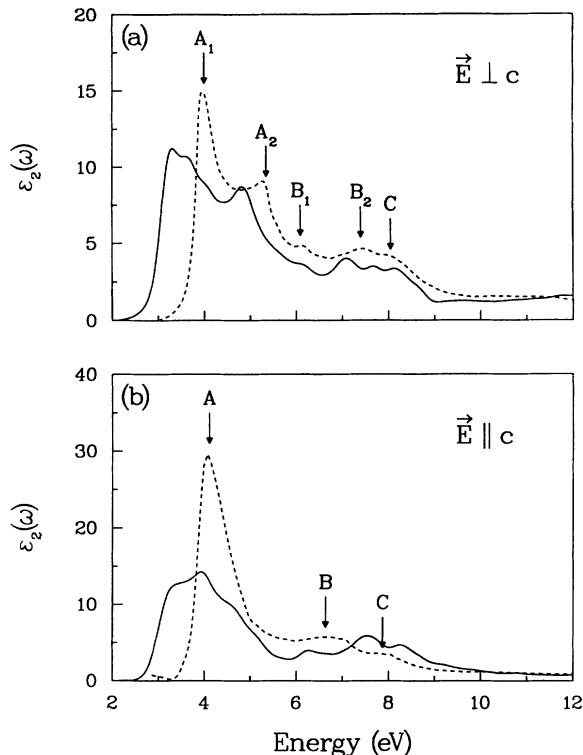

FIG. 14. Imaginary part of the dielectric function for polarization vector (a) perpendicular ($\mathbf{E}_\perp$) and (b) parallel ($\mathbf{E}_\parallel$) to the c axis. Present results (solid line) are compared to the experimental room-temperature results of Cardona and Harbeke (Ref. 94) (dotted lines). Labels correspond to experimentally observed critical points (Ref. 94). Theoretical results have been convoluted with a Gaussian of half-width at half maximum of 0.15 eV to account for finite sampling errors.

compare our theoretical calculations with the experimental results[94] shown by the dashed lines. The corresponding locations of these structural features are given in Table III and compared to the experimental results. As is evident from the shift in the fundamental absorption edge to lower energies, our LDA calculations underestimate the excitation energies. However, beyond the absorption edge, we find good agreement with the experimental fine structure, indicating that a single-particle framework is adequate for this early-transition-metal oxide.

The fundamental absorption edge for $\mathbf{E}_\perp$ occurs at 2.02 eV, resulting from transitions between the topmost valence band and the bottom of the conduction band along the Δ and Σ directions. Beyond the absorption edge, experimental reflectivity[94] and electroreflectance[95] measurements reveal two prominent features, designated as A_1 and A_2 in Fig. 14(a) and Table III, and have been attributed to splitting in the O $2p_{x,y}$ orbitals.[80] The first major peak, which we attribute to A_1, occurs at 3.06 eV and results from transitions between the top of the valence band to the bottom of the conduction band in the neighborhood of the R-A direction. The next major peak, which we assign to A_2, occurs at 4.67 eV and re-

TABLE III. Experimental structure in the imaginary part of the dielectric function of Cardona and Harbeke (Ref. 94) compared to the present first-principles results for polarizations perpendicular $(\mathbf{E}_\perp)$ and parallel $(\mathbf{E}_\parallel)$ to the c axis.

$\mathbf{E}_\perp$	Experiment	Theory	$\mathbf{E}_\parallel$	Experiment	Theory
A_1	4.00	3.06	A	4.11	3.06
A_2	5.35	4.67			
B_1	6.10	6.06	B	6.63	6.15
B_2	7.40	6.96			
C	8.05	7.59	C	7.87	7.27

sults from transitions between the top four valence bands and the t_{2g} conduction-band states, corresponding to the first six conduction bands, in the neighborhood of Γ. Between these two peaks, we find two additional features which have not been observed experimentally.[94] The first feature appears at 3.6 eV, resulting from transitions between valence bands 14 and 15 to the first two conduction bands along the Σ direction near Γ. (We label the valence bands from 1 to 16 and the conduction bands from 1 upwards.) The second feature occurs at 3.94 eV and results from transitions between valence bands 14 and 15 to the lowest three conduction-band states in the neighborhood of the Σ direction. The predicted separation between the A_1 and A_2 peaks was found to be 1.7 eV, which is in good agreement with the experimental value of 1.4 eV.[94] Three other structural features, labeled B_1, B_2, and C in Fig. 14(a) and Table III, have been observed experimentally at higher energies. We find similar high-energy structural features; the first occurring at 6.06 eV is attributed to B_1. The majority of the structure occurs for transitions between valence bands 10–12 and the bottom five conduction-band states of t_{2g} symmetry, as well a transition from valence band 15 to the first conduction-band state of e_g symmetry. These transitions occur in the neighborhood of the Z-A direction. The next high-energy structure is associated with B_2 and occurs at 6.96 eV, resulting from transitions between valence bands 14–16 and the first two conduction bands of e_g symmetry in the neighborhood of Γ. The next structure, attributed to C, occurs at 7.59 eV, and results from transitions between valence bands 11 and 12 and the first two conduction bands of e_g symmetry in the neighborhood of the T direction. We find an additional feature at 8.11 eV resulting from two critical points. The first, near Γ, results from transitions between valence bands 14 and 15 to conduction band 10. The second critical point occurs near A and results from transitions between valence bands 10 and 11 and conduction bands 7 and 8.

The absorption edge, for $\mathbf{E}_\parallel$ polarization, occurs at 2.05 eV and results from transitions between the top of the valence band and the bottom of the conduction band, with the majority of the structure occurring along the Δ direction and minor contributions along Λ. As seen in Fig. 14(b), only one prominent feature, labeled A, has been observed experimentally[94,95] for $\mathbf{E}_\parallel$ and has been attributed to transitions from the O $2p_z$ orbitals.[80] Unlike the case of $\mathbf{E}_\perp$ polarization, where a sharp absorption edge is obtained, we find a rather broad A peak for $\mathbf{E}_\parallel$ as compared to experiment. This is often the case in com-

paring theoretical to experimental results, as excitons can strongly modified the structural features of the absorption edge.[93] Although absorption experiments[80] clearly reveal exciton behavior for the direct-forbidden transition, they are only weakly allowed for $\mathbf{E}_\perp$ and are strictly forbidden for $\mathbf{E}_\parallel$ polarization.[80] This suggests that peak contributions are prominently due to interband transitions rather than excitonic behavior. The first major peak for $\mathbf{E}_\parallel$ polarization occurs at 3.06 eV and results from two critical points. The first, near Γ, is a result of transitions between valence band 14 to the bottom of the conduction band. The second critical point occurs near R and results from transitions from the top of the valence band to the bottom of the conduction band. The second major peak occurs at 3.9 eV and results from transitions between the top four valence bands and the lowest four conduction bands along the Σ and Y directions near M. Two other features on the high-energy side of this peak appear as shoulders at 4.47 and 4.67 eV, respectively, and result from transitions from valence bands 12 and 13 to conduction bands 2 and 4 along Δ. The next major feature appears at 6.15 eV, resulting from the transition from valence bands 11 and 12 to conduction bands 3–5 with t_{2g} symmetry and from valence band 15 to conduction band 7 with e_g symmetry. The transitions are located near the neighborhood of the Z-A-R face and are associated with B. The next major peak occurs at 7.27 eV and is a result of transitions between valence bands 12–14 and conduction bands 7 and 8 located in the neighborhood of the M-Z direction and is associated with C. We find an additional peak composed of two critical points at 8.07 and 8.25 eV resulting from transitions from valence bands 14 and 15 to conduction band 10 near Γ along the Δ and Σ directions and from valence bands 10–12 to conduction bands 7 and 8 in the neighborhood of the Z-R direction.

The real part of the imaginary dielectric function ϵ_1 was calculated using a Kramers-Kronig transformation,[93] where

$$\epsilon_1(\omega) = 1 + \frac{2}{\pi} P \int_0^\infty \frac{\omega' \epsilon_2(\omega')}{\omega'^2 - \omega^2} d\omega', \tag{2}$$

where the P indicates the principal value. In Fig. 15, we compare the theoretical ϵ_1 spectrum to the experimental results of Cardona and Harbeke[94] obtained from their reported extinction and refractive indexes. The static dielectric constant may be obtained from Eq. (2) in the $\omega \to 0$ limit, where we obtain values of 7.3 and 6.4 for $\mathbf{E}_\parallel$ and $\mathbf{E}_\perp$ polarizations, respectively; these are in fairly good
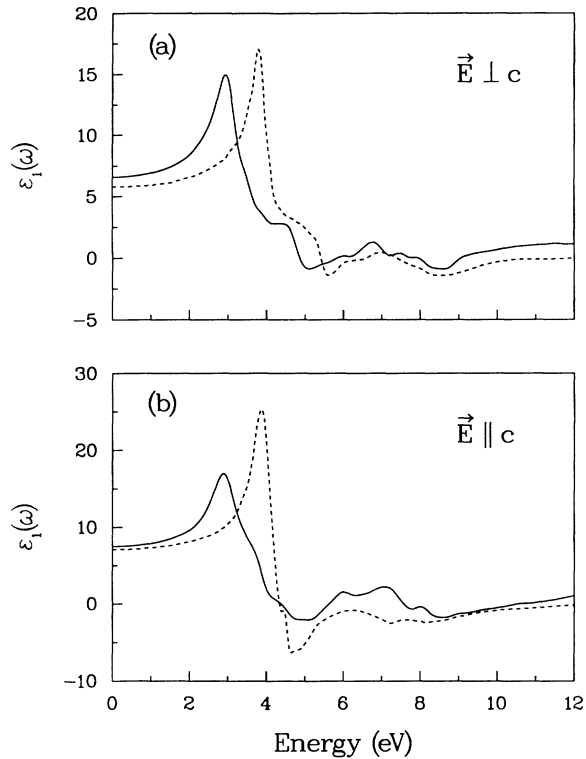
FIG. 15. Real part of the dielectric function for polarization vector (a) perpendicular ($E_\perp$) and (b) parallel ($E_\parallel$) to the c axis. Present results (solid line) are compared to the experimental room-temperature results of Cardona and Harbeke (Ref. 94) (dotted lines). Theoretical results have been convoluted with a Gaussian of half-width at half maximum of 0.15 eV to account for finite sampling errors.

FIG. 16. Reflectivity spectra for polarization vector (a) perpendicular ($E_\perp$) and (b) parallel ($E_\parallel$) to the c axis. Present results (solid line) are compared to the experimental room-temperature results of Cardona and Harbeke (Ref. 94) (dotted lines). Labels correspond to experimentally observed critical points (Ref. 94). Theoretical results have been convoluted with a Gaussian of half-width at half maximum of 0.15 eV to account for finite sampling errors.

agreement with the corresponding experimental[94] room-temperature results of 7.07 and 5.80, respectively. Our theoretical values are somewhat higher than experiment by $\approx 10\%$, as expected, due to the underestimation of the optical band gap.

The normal incident reflectivity $R(\omega)$ was calculated from the dielectric function using the relation $R = |(\sqrt{\epsilon}-1)/(\sqrt{\epsilon}+1)|^2$. The reflectivity is shown in Figs. 16(a) and 16(b) for $E_\perp$ and $E_\parallel$ polarizations, respectively. Also shown in these figures are the experimentally results of Cardona and Harbeke.[94]

VI. SUMMARY AND CONCLUSIONS

We have self-consistently calculated the structural and electronic properties of TiO_2 in the rutile structure. Calculations have been performed within the LDA formalism using *ab initio* pseudopotentials and a plane-wave basis. The ground-state structural and cohesive properties have been determined by self-consistently minimizing the total energy of the system with respect to the structural parameters a, c, and u. Our calculated structural parameters are within 1% of experimentally
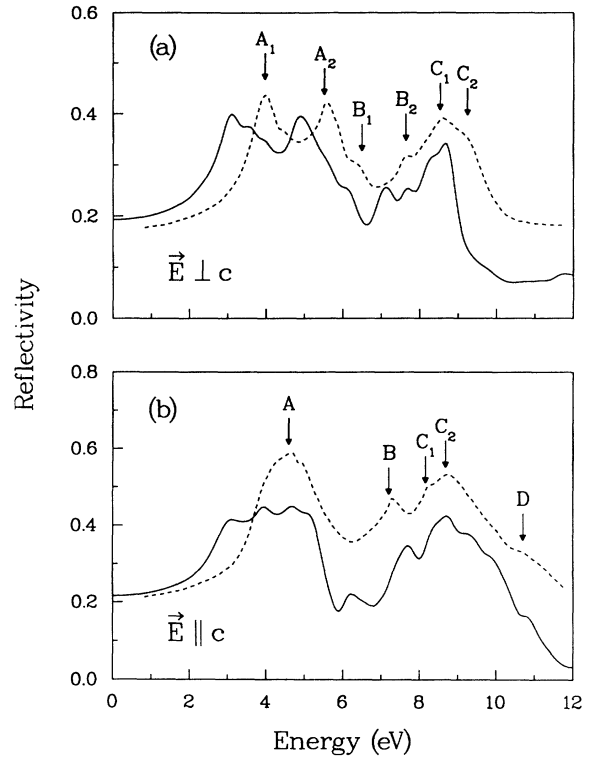
determined values. The cohesive energy was found to be $\sim 5\%$ larger than the experimental value, as is typical of many LDA calculations. We have examined pressure variations in the structural and elastic properties. We find good agreement with the variation of structural properties under pressure, as well as the bulk modulus, Poisson ratio, and the linear compressibilities both perpendicular and parallel to the c axis. While good agreement with experiment is found for the bulk modulus, we find a rather large discrepancy with its pressure derivative, which may be attributed partially to experimental difficulties in pressure measurements.

Valence electron densities have been calculated for high-symmetry planes containing the Ti-O bonds. We obtain qualitative agreement with experimental electron-deformation maps determined by x-ray diffraction. Specifically, we find a large degree of covalent character in the Ti-O bonds, which is also observed in experimental results.

The electronic band structure has been calculated along high-symmetry directions of the irreducible BZ. Our calculated band structure is consistent with various spectroscopies such as XPS, UPS, EELS, etc. for both valence- and conduction-band widths. The correspond-

ing structural features of the density of states are in good agreement with spectroscopic experiments for both ground and excited states. In order to further probe these states, we have performed a detailed analysis of the optical properties of TiO_2. Calculations have been performed for the real and imaginary parts of the dielectric function and the reflectivity spectrum. Structural features in the optical spectra are found to agree well with experimental results above the absorption edge. Sp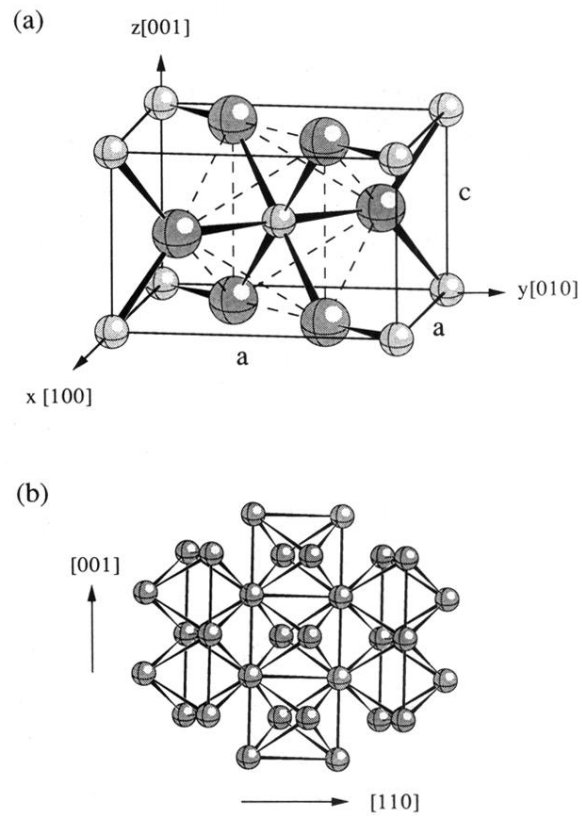ecifically, we are able to account for differences in the electronic polarizations, suggesting that for this early-transition-metal oxide, its optical matrix elements can be accurately described within the LDA.

ACKNOWLEDGMENTS

[1]F. A. Grant, Rev. Mod. Phys. **31**, 646 (1959).

[2]J. B. Goodenough, Prog. Solid State Chem. **5**, 145 (1971).

[3]V. E. Henrich, Rep. Prog. Phys. **48**, 1481 (1985).

[4]P. Hohenberg and W. Kohn, Phys. Rev. **136**, B864 (1964); W. Kohn and L. J. Sham, *ibid.* **140**, A1133 (1965).

[5]*Theory of the Inhomogeneous Electron Gas,* edited by S. Lundqvist and N. H. March (Plenum, New York, 1983).

[6]W. E. Pickett, Comput. Phys. Rep. **9**, 115 (1989).

[7]R. O. Jones and O. Gunnarsson, Rev. Mod. Phys. **61**, 689 (1989).

[8]O. H. Nielsen and R. M. Martin, Phys. Rev. Lett. **50**, 697 (1983); Phys. Rev. B **32**, 3780 (1985); **32**, 3792 (1985).

[9]S. Fahy, X. W. Wang, and S. G. Louie, Phys. Rev. Lett. **61**, 1631 (1988).

[10]J. Ihm, A. Zunger, and M. L. Cohen, J. Phys. C **12**, 4409 (1979); **13**, 3095 (1980).

[11]J. L. Martins, N. Troullier, and S.-H. Wei, Phys. Rev. B **43**, 2213 (1991).

[12]R. Car and M. Parrinello, Phys. Rev. Lett. **55**, 2471 (1985).

[13]M. S. Hybertsen and S. G. Louie, Phys. Rev. Lett. **55**, 1418 (1985); Phys. Rev. B **34**, 5390 (1986), and references cited therein.

[14]N. Troullier and J. L. Martins, Solid State Commun. **74**, 613 (1990); Phys. Rev. B **43**, 1993 (1991).

[15]A. M. Rappe, K. M. Rabe, E. Kaxiras, and J. D. Joannopoulos, Phys. Rev. B **41**, 1227 (1990).

[16]D. Vanderbilt, Phys. Rev. B **32**, 8412 (1985).

[17]J. L. Martins and M. L. Cohen, Phys. Rev. B **37**, 6134 (1988).

[18]S. J. Tauster, S. C. Fung, and R. L. Garten, J. Am. Chem. Soc. **100**, 170 (1978).

[19]D. J. Dwyer, S. D. Cameron, and J. Gland, Surf. Sci. **159**, 430 (1985).

[20]A. Fujishima and K. Honda, Nature **238**, 37 (1972); S. Sato and J. M. White, J. Phys. Chem. **85**, 592 (1981).

[21]L. Liu and W. A. Bassett, *Elements, Oxides, and Silicates* (Oxford University Press and Clarendon, New York, 1986), p. 115, and references cited therein.

[22]H. Sato, S. Endo, M. Sugiyama, T. Kikegawa, O. Shimomura, and K. Kusaba, Science **251**, 786 (1991).

[23]D. M. Ceperley and B. J. Adler, Phys. Rev. Lett. **45**, 566 (1980).

[24]J. P. Perdew and A. Zunger, Phys. Rev. B **23**, 5048 (1981).

[25]M. T. Yin and M. L. Cohen, Phys. Rev. B **26**, 5668 (1982).

[26]M. T. Yin and M. L. Cohen, Phys. Rev. Lett. **50**, 2006 (1983).

[27]J. R. Chelikowsky and S. G. Louie, Phys. Rev. B **29**, 3470 (1984).

[28]J. R. Chelikowsky, S. G. Louie, D. Vanderbilt, and C. T. Chan, Int. J. Quantum Chem. Symp. **18**, 105 (1984).

[29]J. R. Chelikowsky, C. T. Chan, and S. G. Louie, Phys. Rev. B **34**, 6656 (1986).

[30]O. Gunnarsson, J. Harris, and R. O. Jones, J. Chem. Phys. **67**, 3970 (1977); M. Y. Chou and J. R. Chelikowsky, Phys. Rev. Lett. **59**, 1737 (1987).

[31]L. Kleinman and D. M. Bylander, Phys. Rev. Lett. **48**, 1425 (1982).

[32]X. Gonze, P. Käckell, and M. Scheffler, Phys. Rev. B **41**, 12 264 (1990); D. R. Hamann, *ibid.* **40**, 2980 (1989); X. Gonze, R. Stumpf, and M. Schleffer, *ibid.* **44**, 8503 (1991); D. M. Bylander and L. Kleinman, *ibid.* **41**, 907 (1990).

[33]J. F. Banfield, D. R. Veblen, and D. J. Smith, Am. Mineral. **76**, 343 (1991).

[34]L. Pauling, J. Am. Chem. Soc. **51**, 1010 (1929).

[35]S. C. Abrahams and J. L. Bernstein, J. Chem. Phys. **55**, 3206 (1971).

[36]C. J. Howard, T. M. Sabine, and F. Dickson, Acta. Crystallogr. Sec. B **47**, 462 (1991), and references cited therein.

[37]M. O'Keefe, Acta Crystallogr. Sec. A **33**, 924 (1977).

[38]O. Gunnarsson, B. I. Lundqvist, and J. W. Wilkins, Phys. Rev. B **10**, 1319 (1974).

[39]F. D. Murnaghan, Proc. Natl. Acad. Sci. U.S.A. **30**, 244 (1944).

[40]F. Birch, J. Geophys. Res. **57**, 227 (1952).

[41]P. Vinet, J. Ferrante, J. R. Smith, and J. H. Rose, J. Phys. C **19**, L467 (1986); J. Geophys. Res. **92B**, 9319 (1987).

[42]*CRC Handbook of Chemistry and Physics,* 64th ed. (CRC, Boca Raton, FL, 1983).

[43]C. Kittel, *Introduction to Solid State Physics,* 6th ed. (Wiley, New York, 1986).

[44]J. K. Burdett, T. Hughbanks, G. J. Miller, J. W. Richardson, Jr., and J. V. Smith, J. Am. Chem. Soc. **109**, 3639 (1987).

[45]M. H. Manghnani, J. Geophys. Res. **74**, 4317 (1969); M. H. Manghnani, E. S. Fisher, and W. S. Brower, Jr., J. Phys. Chem. Solids **33**, 2149 (1972).

[46]I. J. Fritz, J. Phys. Chem. Solids **35**, 817 (1974).

[47]R. G. McQueen, J. C. Jamieson, and S. P. Marsh, Science **155**, 1401 (1967).

[48]L. Ming and M. H. Manghnani, J. Geophys. Res. **84B**, 4777 (1979).

[49]Y. Sato, in *High-Pressure Research: Applications in Geophysics,* edited by M. H. Manghnani and S. Akimoto (Academic, New York, 1977), p. 307.

[50]T. Mashimo, K. Nagayama, and A. Sawaoka, J. Appl. Phys. **54**, 5043 (1983).

[51]Y. Syono, K. Kusaba, M. Kikuchi, K. Fukuoka, and T. Goto, in *High-Pressure Research in Mineral Physics,* edited by M. H. Manghnani and Y. Syono (Terra Scientific, Tokyo, 1987), p. 385.

[52]R. M. Hazen and L. W. Finger, J. Phys. Chem. Solids **42**, 143 (1981).

[53]B. G. Hyde, Z. Kristallogr. **179**, 205 (1987).

[54]W. Göpel, J. A. Anderson, D. Frankel, M. Jaehnig, K. Phillips, J. A. Schäfer, and G. Rocker, Surf. Sci. **139**, 333 (1984).

[55]S. Hüfner and G. K. Wertheim, Phys. Rev. B **8**, 4857 (1973).

[56]S. P. Kowalczyk, F. R. McFeely, L. Ley, V. T. Gritsyna, and D. A. Shirley, Solid State Commun. **23**, 161 (1977).

[57]M. L. Knotek and P. J. Feibelman, Phys. Rev. Lett. **40**, 964 (1978).

[58]D. W. Fischer, Phys. Rev. B **5**, 4219 (1972).

[59]K. Tsutsumi, O. Aita, and K. Ichikawa, Phys. Rev. B **15**, 4638 (1977).

[60]F. M. F. de Groot, M. Grioni, J. C. Fuggle, J. Ghijsen, G. A. Sawatzky, and H. Petersen, Phys. Rev. B **40**, 5715 (1989).

[61]G. van der Laan, Phys. Rev. B **41**, 12 366 (1990); G. van der Laan, C. S. Mythen, and H. A. Padmore, Europhys. Lett. **11**, 67 (1990).

[62]L. A. Grunes, Phys. Rev. B **27**, 2111 (1983).

[63]R. Brydson, H. Sauer, W. Engel, J. M. Thomas, E. Zeitler, N. Kosugi, and H. Kuroda, J. Phys. Condens. Matter **1**, 797 (1989); R. Brydson, B. G. Williams, W. Engel, H. Sauer, E. Zeitler, and J. M. Thomas, Solid State Commun. **64**, 609 (1987).

[64]M. H. Mohamed, H. R. Sadeghi, and V. E. Henrich, Phys. Rev. B **37**, 8417 (1988).

[65]L. A. Grunes, R. D. Leapman, C. N. Wilker, R. Hoffmann, and A. B. Kunz, Phys. Rev. B **25**, 7157 (1982).

[66]R. H. Tait and R. V. Kasowski, Phys. Rev. B **20**, 5178 (1979).

[67]G. F. Derbenwick (unpublished).

[68]Z. Zhang, S.-P. Jeng, and V. E. Henrich, Phys. Rev. B **43**, 12 004 (1991).

[69]K. M. Glassford, N. Troullier, J. L. Martins, and J. R. Chelikowsky, Solid State Commun. **76**, 635 (1990).

[70]D. C. Allan and M. P. Teter, J. Am. Ceram. Soc. **73**, 3247 (1990).

[71]B. Silvi, N. Fourati, R. Nada, and C. R. A. Catlow, J. Phys. Chem. Solids **52**, 1005 (1991).

[72]N. I. Medvedeva, V. P. Zhukov, M. Ya. Khodos, and V. A. Gubanov, Phys. Status Solidi B **160**, 517 (1990).

[73]M. A. Khan, A. Kotani, and J. C. Parlebas, J. Phys. Condens. Matter **3**, 1763 (1991).

[74]B. Poumellec, P. J. Durham, and G. Y. Guo, J. Phys. Condens. Matter **3**, 8195 (1991).

[75]J. A. Tossell, D. J. Vaughan, and K. H. Johnson, Am. Mineral. **59**, 319 (1974).

[76]S. Munnix and M. Schmeits, Phys. Rev. B **30**, 2202 (1984).

[77]K. Vos, J. Phys. C **10**, 917 (1977).

[78]N. Daude, C. Gout, and C. Jouanin, Phys. Rev. B **15**, 3229 (1977).

[79]J. K. Burdett, Inorg. Chem. **24**, 2244 (1985).

[80]J. Pascual, J. Camassel, and H. Mathieu, Phys. Rev. Lett. **39**, 1490 (1977); Phys. Rev. B **18**, 5606 (1978).

[81]F. Arntz and Y. Yacoby, Phys. Rev. Lett. **17**, 857 (1966).

[82]J. H. Becker and W. R. Hosler, J. Phys. Soc. Jpn. **18**, Suppl. II, 152 (1963); Phys. Rev. **137**, A1872 (1965).

[83]G. A. Acket and J. Volger, Physica **32**, 1680 (1966).

[84]G. L. Bir, V. N. Bogomolov, E. V. Krivitskii, and T. E. Sulyatitskaya, Fiz. Tverd. Tela (Leningrad) **7**, 2978 (1966) [Sov. Phys. Solid State **7**, 2414 (1966)].

[85]D. C. Cronemeyer, Phys. Rev. **87**, 876 (1952).

[86]H. Mathieu, J. Pascual, and J. Camassel, Phys. Rev. B **18**, 6920 (1978); J. Camassel, J. Pascual, and H. Mathieu, *ibid.* **20**, 5292 (1979).

[87]R. V. Kasowski and R. H. Tait, Phys. Rev. B **20**, 5168 (1979).

[88]B. Poumellec, J. F. Marucco, and B. Touzelin, Phys. Rev. B **35**, 2284 (1987).

[89]J. H. Xu, T. Jarlborg, and A. J. Freeman, Phys. Rev. B **40**, 7939 (1989).

[90]G. Lehmann and M. Taut, Phys. Status Solidi **54**, 469 (1972); O. Jepsen and O. K. Anderson, Solid State Commun. **9**, 1763 (1971).

[91]L. Pauling, *The Nature of the Chemical Bond* (Cornell University, Ithaca, 1945).

[92]R. Restori, D. Schwarzenbach, and J. R. Schneider, Acta. Crystallogr. Sec. B **43**, 251 (1987).

[93]M. L. Cohen and J. R. Chelikowsky, in *Electronic Structure and Optical Properties of Semiconductors,* 2nd ed., edited by M. Cardona (Springer-Verlag, Berlin, 1989).

[94]M. Cardona and G. Harbeke, Phys. Rev. **137**, A1467 (1965).

[95]A. Frova, P. J. Boddy, and Y. S. Chen, Phys. Rev. **157**, 700 (1967).

[96]K. Vos and H. J. Krusemeyer, Solid State Commun. **15**, 949 (1974); J. Phys. C **10**, 3893 (1977).

[97]J. P. Perdew and M. Levy, Phys. Rev. Lett. **51**, 1884 (1983).

[98]A. Svane and O. Gunnarsson, Phys. Rev. Lett. **65**, 1148 (1990).

[99]R. A. Heaton, J. G. Harrison, and C. C. Lin, Solid State Commun. **41**, 827 (1982); Phys. Rev. B **28**, 5992 (1983).

[100]H. Ehrenreich and M. H. Cohen, Phys. Rev. **115**, 786 (1959).

[101]S.-Y. Ren and W. A. Harrison, Phys. Rev. B **23**, 762 (1981).

[102]V. P. Gupta and N. M. Ravindra, J. Phys. Chem. Solids **41**, 591 (1980).

(a)

z[001]

c

y[010]

a

a

x [100]

(b)

[001]

[110]

FIG. 3. Primitive unit cell for TiO_2 in the rutile structure (a); larger spheres represent the O atoms and the smaller Ti. In (b), we illustrate the connectivity of the oxygen octahedra projected onto the (110) plane; the Ti atoms have been omitted for clarity.